

Formation of Ionization-Cone Structures in Active Galactic Nuclei: II. Nonlinear Hydrodynamic Modelling

V. L. Afanasiev¹, S. N. Dodonov¹, S. S. Khrapov², V. V. Mustsevoi², A. V. Moiseev¹

¹ Special Astrophysical Observatory, RAS, Nizhnii Arkhyz, Karachai-Cherkessian Republic, 357147 Russia

² Volgograd State University, Volgograd, 400062 Russia

received: September 21, 2006/ revised: November 24, 2006

Abstract. In Part I of this paper we described an equilibrium model of a jet in the gravitational field corresponding to the rigid-rotation region of the galactic disk. We used linear stability analysis to find the waveguide-resonance instability of internal gravity waves due to the superreflection of these waves from the jet boundary. In this part of the paper, we perform nonlinear numerical 2D and 3D simulations of the development of this instability. We show that the shocks produced by this instability in the ambient medium of the jet are localized inside a cone with a large opening angle and are capable of producing features that are morphologically similar to those observed in galaxies with active nuclei (NGC 5252 for example).

1. Introduction

In Paper I (Afanasiev et al., 2007) we used linear stability analysis to investigate the possibility of the formation of regular structures resulting from the development of hydrodynamic instabilities in conical jets including those with large opening angles. At the same time, the very existence of such weakly collimated jet outflows from active galactic nuclei raises certain doubts — observed formations are widely believed to be radiation cones and not mass outflows (see the “Introduction” section in Paper I). From purely hydrodynamic viewpoint it is not quite clear why in such similar accretion-jet objects protostellar systems develop highly collimated jets, whereas active galactic nuclei produce wide-angle cone outflows. Note that it is extremely difficult to determine from observations whether we are dealing with a highly collimated or large-opening-angle conical outflow. This is due to the fact that jets from active galactic nuclei are almost without exception observed through high-intensity shocks produced by the intrusion of the outflow matter into the unperturbed ambient medium (Falcke et al., 1996, Nagar et al., 1999). Hence a significant number of shock-excited ions is present along the line of sight in any case.

In this paper we analyze a situation that is alternative to that addressed in Paper I. In our case, the jet outflow from the nucleus is collimated, but the nonlinear stage of the development of instability in the jet results in the localization of the resulting shocks inside a wide cone. We believe that this effect can explain the formation of struc-

tures observed in the vicinity of Seyfert nuclei (Z-shaped “arms”, “arcs”, and “arches” — see Paper I). Note that Hardee (1982), Falcke et al. (1996) and Lobanov et al. (2006) already pointed out the possibility of the formation of such structures in the vicinity of active nuclei due to the interaction of radio-jet matter with the ambient medium in the boundary layer.

Section 2 describes the technique of numerical simulations, Section 3 discusses the results of these simulations and proves that perturbations that build up in the jet as a result of waveguide-resonance instability produce in the ambient medium a system of intensely radiating nonlinear waves. Section 4 summarizes the main conclusions and gives the final comments.

2. Technique of numerical simulations

The stationary model that we use in this part of the work is quite similar to that described in Paper I. The only exceptions are the numerical parameter values that we give at the end of this section.

2.1. Basic Equations

In our numerical simulations of the dynamics of perturbations we use the following set of hydrodynamics equations in divergent form written in the spherical coordinate system (r, θ, φ) :

$$\frac{\partial \rho}{\partial t} + \text{div}(\rho \mathbf{V}) = 0, \quad (1)$$

$$\frac{\partial(\rho U)}{\partial t} + \text{div}(\rho U \mathbf{V}) = -\frac{\partial p}{\partial r} + \rho \left(\frac{|\mathbf{V}|^2}{r} - \frac{\partial \Psi}{\partial r} \right), \quad (2)$$

$$\frac{\partial(r\rho W)}{\partial t} + \text{div}(r\rho W \mathbf{V}) = -\frac{\partial p}{\partial \theta} + \rho V^2 \text{ctg}\theta, \quad (3)$$

$$\frac{\partial(r \sin \theta \rho V)}{\partial t} + \text{div}(r \sin \theta \rho V \mathbf{V}) = -\frac{\partial p}{\partial \varphi}, \quad (4)$$

$$\begin{aligned} \frac{\partial E}{\partial t} + \text{div}[\mathbf{V}(E+p)] = \\ -\rho U \frac{\partial \Psi}{\partial r} + C_{\Gamma} \rho \varepsilon - C_{\Lambda} \rho^2 \varepsilon^{5/2}, \end{aligned} \quad (5)$$

where

$$\text{div} \mathbf{V} = \frac{1}{r^2} \frac{\partial}{\partial r}(r^2 U) + \frac{1}{r \sin \theta} \frac{\partial}{\partial \theta}(\sin \theta W) + \frac{1}{r \sin \theta} \frac{\partial V}{\partial \varphi},$$

ρ is the density; p , the pressure; $\mathbf{V} = (U, W, V)$, the velocity vector; $E = \rho \frac{|\mathbf{V}|^2}{2} + \frac{p}{(\gamma-1)}$, the total energy, and $\varepsilon = \frac{p}{(\gamma-1)\rho}$, the internal energy per unit mass.

2.2. Numerical Scheme and Boundary Conditions

We numerically integrate equation set (1)–(5) using the TVD–E scheme (Ryu et al., 1993) adapted to the spherical coordinate system with a variable radial step.

To analyze the dynamics of axisymmetric perturbations, we use a two-dimensional (2D) scheme (r, θ) with integration domain $(r_{in} \leq r \leq r_{ex}$ and $0 \leq \theta \leq \pi/2)$ containing a total of $N_r \times N_{\theta}$ cells. To analyze the dynamics of nonaxisymmetric perturbations, we use a three-dimensional (3D) scheme (r, θ, φ) with integration domain $(r_{in} \leq r \leq r_{ex}; 0 \leq \theta \leq \pi/2; 0 \leq \varphi \leq 2\pi)$ containing a total of $N_r \times N_{\theta} \times N_{\varphi}$ cells.

It follows from linear analysis (Paper I) that the perturbation wavelength increases linearly with distance, because $kr = \text{const}$. Accordingly, in our numerical simulations we use a variable step in radial coordinate $\Delta r_{i+1} = e^{\Delta x} \Delta r_i$, where $\Delta x = (\ln r_{ex} - \ln r_{in})/N_r$. With Δr so defined, the number of cells per wavelength remains constant along the radius. We set constant integration steps in the θ and φ directions, i.e., $\Delta \theta = \pi/2N_{\theta}$, $\Delta \varphi = 2\pi/N_{\varphi}$.

To avoid distortions in the (r, θ) plane due to the differences between the scheme velocities of the propagation of perturbations in the r and θ directions, Δr_i and $r_i \Delta \theta$ cells should have equal lengths in these directions. I.e., $\Delta x = \Delta \theta$ and $N_r = 2N_{\theta} (\ln r_{ex} - \ln r_{in})/\pi$.

For unstable modes to build up in numerical simulations, a finite-width transition layer is required between the jet matter and the ambient medium (see Paper I). We set the extent of the transition layer by setting the size of the cell in the θ -direction. In this case, the thickness of the transition layer decreases with increasing N_{θ} . The equilibrium distributions in the transition layer have the following form:

$$\begin{aligned} U_s(r) &= U_j(r)/2, \\ \rho_s(r) &= \frac{\tilde{R} \rho_j(r) r^2}{\Omega^2 r^2 + U_j^2(r)/4}, \end{aligned}$$

Fig. 1. Radial dependences of relative perturbations (the solid bold, solid, dashed, and dashed-and-dotted lines correspond to ρ , U , p , and W , respectively) for $\theta = \theta_j$ at different time instants: $t = 0.5$ (top) and $t = 1$ (bottom). Large amplitudes correspond to the $n_j = 0$ harmonic of the waveguide-resonance mode and lower amplitudes, to the Kelvin-Helmholtz mode.

$$p_s(r) = p_j(r) = p_a(r),$$

where subscripts “j”, “a”, and “s” refer to the jet, ambient medium, and transition layer, respectively, and U_j and U_s are the radial velocities of gas flow in the equilibrium state.

We set the initial perturbation of the θ component in the following form:

$$\begin{aligned} \tilde{W}(r, \theta, \varphi) &= \Delta_w \sin(kr \ln r + m \varphi) \\ &\times \exp \left\{ - \left(\frac{\sin \theta - \sin \theta_j}{\delta} \right)^2 \right\}, \end{aligned}$$

where Δ_w is the initial perturbation amplitude ($\Delta_w \ll U_j$); kr , the dimensionless wavenumber, and m , the number of azimuth mode. We set the scale factor δ equal to 0.2.

We use the following boundary condition.

- In the symmetry plane of the system ($\theta = \pi/2$): symmetric boundary conditions $f(\pi/2 - 0) = f(\pi/2 + 0)$ for E , ρ , U , and V , and antisymmetric boundary conditions $f(\pi/2 - 0) = -f(\pi/2 + 0)$ for W .
- At the symmetry axis of the system ($\theta = 0$): 2D scheme — symmetric boundary conditions $f(-0) = f(+0)$ for E , ρ , and U and antisymmetric boundary conditions $f(-0) = -f(+0)$ for W ; 3D-scheme — $f(r, -0, \varphi) = f(r, +0, \varphi + \pi)$.
- At $\varphi = 0$ and $\varphi = 2\pi$: periodic boundary conditions — $f(-0) = f(2\pi - 0)$, $f(2\pi + 0) = f(+0)$.
- At the inner ($r = r_{in}$) and outer ($r = r_{ex}$) radial boundaries:

$$\begin{aligned} f(r_{in} - 0) &= f_0(r_{in} - 0) + \tilde{f}(r_{in} + \lambda) \frac{B_f(r_{in} - 0)}{B_f(r_{in} + \lambda)}, \quad f(r_{ex} + 0) = \\ &f_0(r_{ex} + 0) + \tilde{f}(r_{ex} - \lambda) \frac{B_f(r_{ex} + 0)}{B_f(r_{ex} - \lambda)}, \end{aligned}$$

where $B_f(r)$ is the amplitude function (envelope of perturbations) and λ , the perturbation wavelength. Subscript “0” indicates the equilibrium values. According to the results of linear analysis (Paper I), the amplitude function at the initial time instant is $B_f(r) = r^{\beta_f}$. At subsequent time instants B_f can be computed by approximating the minima and maxima of perturbations in the grid cells.

2.3. Parameter Values and the Transition to Dimensionless Variables

The dimensionless parameter $\tau = t_{dyn}/t_{rad}$ that describes the intensity of radiative cooling is determined by the ratio of two time scales of the problem: the dynamic

Fig. 2. Time dependences of the logarithms of density perturbation amplitudes: the curves of families 1 and 2 correspond to $\theta = \theta_j$ and $\theta = 1.5\theta_j$, respectively. The middle, lower, and upper curves of each family on the upper panel correspond to $r(N_r/2)$, $r(3N_r/4)$, and $r(N_r/4)$, respectively. The solid curves in the lower panel were computed with a 256×128 grid and the dashed curves, on a 128×64 grid.

time scale t_{dyn} and radiative cooling time scale t_{rad} . Here $t_{dyn} = r \sin \theta_j / c_j$ is the time scale of the propagation of perturbations from the boundary to the symmetry axis of the jet ($\theta = 0$), and $t_{rad} = p / [(\gamma - 1) C_{\Lambda} \rho^2 \varepsilon^{5/2}]$ is the time during which the energy of gas decreases by a factor of e due to radiative cooling. At $\tau \ll 1$ the effect of radiative cooling has a negligible effect on the dynamics of perturbations (Paper I). At $\tau \geq 1$ radiative cooling plays an important part in the evolution of unstable modes.

We do not take into account the processes connected to viscosity and heat conductivity because the basic estimates show that the ratio of the dynamical time to the characteristic time of such processes has the order $\text{Kn}/M \ll 1$, where Kn is the Knudsen number and M is the Mach number.

We performed simulations for $\gamma = 5/3$, $\tau = 2$ or $\tau = 4$, jet half-opening angles $\theta_j = 5^\circ$ or $\theta_j = 10^\circ$ and the jet-to-ambient medium pressure ratio of $\tilde{R} = 5$ or $\tilde{R} = 10$.

In accordance with the results of Paper I, we set the Mach number of the outflow equal to $M \simeq 0.69$ or $M \simeq 0.74$. For the initial perturbations, we set $kr = 16$ and $\Delta_w = 10^{-9}$ or $\Delta_w = 10^{-8}$. We find no qualitative differences between the results of the two series and therefore below we describe the simulations with $\Delta_w = 10^{-8}$. The results of the series of the numerical simulations have shown that harmonics with $kr = 16$ grow most quickly, it is only these harmonics that we show in the figures.

Note that we had to set such a relatively large jet opening angle because of the limited potential of the computers employed. For perturbations to be processed correctly, the half-opening angle must contain at least 10 cells of the computation domain, whereas we could not increase N_θ appreciably because of the limited RAM of the computers employed.

Dimensionless boundaries of the computational domain were determined by the $\tilde{r}_{in} = 1$ and $\tilde{r}_{ex} = e^\pi$ values. In accordance with Paper I, we perform our analysis for the radii corresponding to the rigid-rotation region of the galactic disk with the angular velocity $\Omega \simeq 100 - 300 \text{ km s}^{-1} \text{ kpc}^{-1} = \text{const}$ (which corresponds to the region inside the bulge).

The outer boundary in dimensionless units is equal to $r_{ex} \simeq (0.5 - 3) \text{ kpc}$ and the inner boundary is e^π times smaller, $r_{in} \simeq (22 - 130) \text{ pc}$, depending on the specifics of the rotation curves of real galaxies.

Concerning the transition to dimensionless velocities, let us point out that the balance of pressures in the jet and

Fig. 3. Radial dependences of relative perturbations (ρ (the solid bold line); U (the thin line); p (the dashed line), and W (the dashed-and-dotted line)) at different time instants for $\theta = \theta_j/2$: $t = 2$ (top), $t = 3.2$ (middle), and $t = 7.1$ (bottom).

Fig. 4. Same as Fig. 3, but for $\theta = \theta_j$.

in the ambient medium (equation (4) in Paper I) allows equation (5) of Paper I to be rewritten as:

$$\frac{1}{2} \frac{\partial U_j^2}{\partial r} = \left(\frac{\rho_a}{\rho_j} - 1 \right) \frac{\partial \Psi}{\partial r}. \quad (6)$$

We further take into account that $U_j \propto r$ and the dependence of gravitational potential on radius, in accordance with Paper I, is

$$\Psi = \Psi_0 + \frac{1}{2} \Omega^2 r^2, \quad (7)$$

to find from (6):

$$U_j = \Omega r \sqrt{\frac{\rho_a}{\rho_j} - 1} = \Omega r \sqrt{\tilde{R} - 1}. \quad (8)$$

It is hence natural to normalize velocity to Ωr_{ex} . In this case, the sound speeds in the jet and in the ambient medium are unambiguously determined by the dimensionless parameters M and \tilde{R} . We have for typical galaxies $\Omega r_{ex} \simeq (100 - 300) \text{ km s}^{-1}$, and hence (8) implies that we must be dealing with a high-velocity jet (for the \tilde{R} adopted above, e.g., $U_j = 3\Omega r$) despite the subsonic nature of the flow in this jet ($U_j < c_j$). This is consistent with the conclusion that we made in Paper I that jet matter must be strongly heated by the radiation of the galactic nucleus.

We determined the dimensionless time as $\tilde{t} = t\Omega$. We have $\Omega = (0.1 - 2) \times 10^{-14} \text{ rad s}^{-1}$ and this corresponds to $t = (0.5 - 9) \times 10^{14} \text{ s} = (0.2 - 2.9) \times 10^7 \text{ years}$.

Finally, to pass to dimensionless density, we chose the value $\rho_j(r_{in}) = 6.7 \cdot 10^{-23} \text{ g cm}^{-3}$, which corresponds to number densities $n_j(r_{in}) = 35 \text{ cm}^{-3}$.

3. RESULTS OF NONLINEAR NUMERICAL SIMULATIONS

3.1. Basic Comments

When analyzing the evolution of perturbations, we could make use of higher spatial resolution for axisymmetric modes (2D) and hence reproduce higher-order effects. We therefore begin with the dynamics of pinch ($m = 0$) modes (Section 3.2), and only then discuss three-dimensional helical ($m = 1$) modes (Section 3.3).

Computation of the luminosity and surface density of the simulated structures is associated with the following problems. It is evident from the set of equations (1)–(5) that the real luminosity in individual emission lines cannot be computed because the set includes no equations of

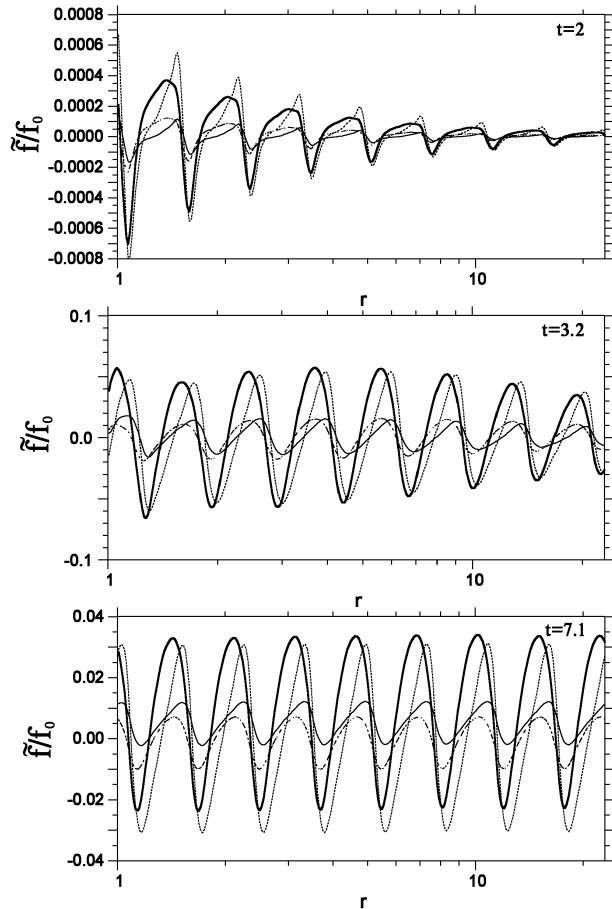


Fig. 5. Same as Fig. 3, but for $\theta = 1.25\theta_j$.

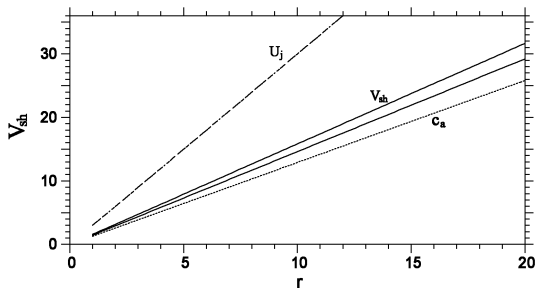


Fig. 6. Velocities of shock fronts at time $\tilde{t} = 7.1$: angles $1.25\theta_j$ (the upper solid line) and $1.5\theta_j$ (the lower solid line). The dashed and dashed-and-dotted lines show the sound speed in the ambient medium (c_a) and the jet velocity (U_j), respectively.

photoionization balance. However, structures discussed in the following sections are observed inside the ionization cones both in Balmer and shock-excited forbidden lines. Our analysis of the simulation results yielded the relative emission-line luminosity of the features of the wave pattern by integrating function $(\rho^2\Lambda(T) - \rho_0^2\Lambda(T_0))/\rho_0^2\Lambda(T_0)$ along the line of sight. In this definition one has to subtract the contribution of hot matter inside the jet from the total radiation. We therefore did not integrate the above function over the cells located inside the jet ($\theta \leq \theta_j$), be-

cause the ionized-gas temperature at these sites is so high that the gas cannot radiate in optical lines and most of its luminosity is contained at X-ray spectral domain.

3.2. Results of 2D Simulation

As we pointed out in Section 2, we performed a set of computations with various parameter values and different numbers of cells in the computational space: $N_r = 128$, $N_\theta = 64, 128, 256$. Careful comparison of eigenfunctions, obtained from the linear analysis, with results of an initial stage of numerical simulations, shows that two unstable modes developed in all the numerical simulations performed: the surface Kelvin-Helmholtz (KHI) mode and the main¹ waveguide-resonance IGW mode of the u^- family. Unlike the latter, the Kelvin-Helmholtz mode proved to be very sensitive to the thickness of the transition layer between the jet and ambient medium, which is determined by the step of the grid cell size in the θ -direction. The stabilizing effect of the velocity shift is a well known fact (see, e.g., Bodo et al., 1989; Mustsevoi V.V. & Khoperskov, 1991). Therefore the KHI mode contributed appreciably to the resulting perturbation pattern only on the $N_\theta = 256$ grid (see Fig. 1), whereas its amplitude was negligible in all other computations.

Figure 2 illustrates the above-mentioned effect of the “thickness” of the transitional layer on the perturbation increment: increment grows with increasing spatial resolution of the grid and asymptotically tends to the value determined from linear analysis of the discontinuous model.

A characteristic feature of the evolution of perturbations in all the computational series performed is that radial dependences of the amplitude envelopes of all quantities can be fitted fairly well by function r^{β_f} (see Section 3 of Paper I). At the same time, at the stage of nonlinear saturation these dependences transform to the form r^{α_f} , which describes equilibrium distributions (see Figs. 3–5).

During the nonlinear stage the development of waveguide-resonance instability of the main ($n_j = 0$) IGWs mode produces shocks in the medium that surrounds the jet with approximately paraboloidal fronts in the real three-dimensional space. Figure 5 shows the radial dependence of the r component of mass velocity at $\theta = 12.5^\circ$. The perturbations discussed here can be seen to be real shocks given the well-known fact that the discontinuity surfaces in computations based on the TVD-E numerical scheme are always “smeared” over at least five spatial cells of the system (Ryu et al., 1993). It is clear from Fig. 5 that the width of the shock in our case is equal to four to six cells, i.e., we indeed observe a discontinuity surface — a shock front — at this location. A comparison of the perturbation propagation velocity v_{sh} in the direction normal to the shock surface with the sound speed c_a in the medium that surrounds the jet corroborates this

¹ I.e., a mode with no eigenfunction zero points between the jet boundary and symmetry axis — $n_j = 0$ (see Paper I).

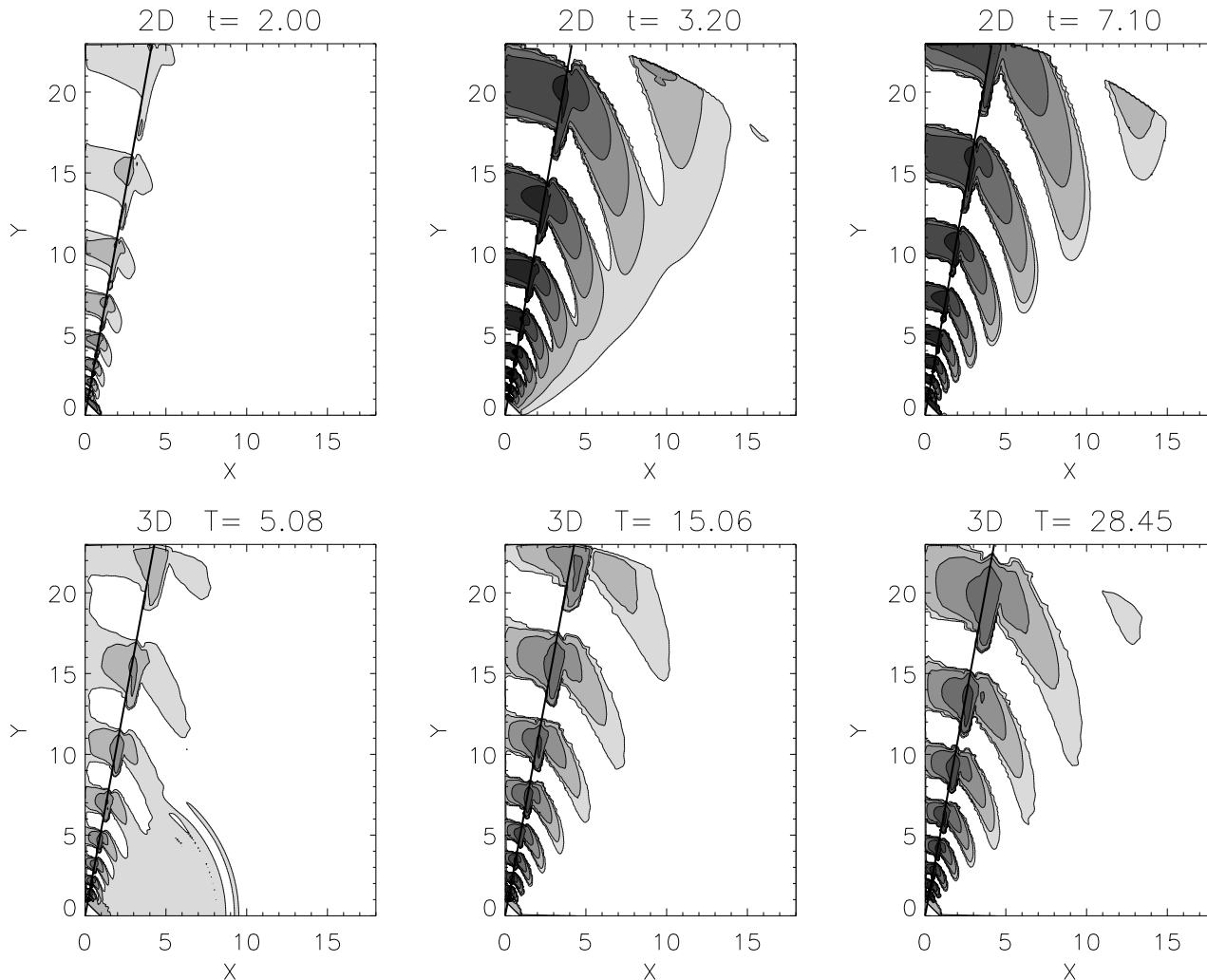


Fig. 7. Luminosity contours for the two- (figures at the top) and three-dimensional (figures at the bottom) simulations in the $(x = r \sin \theta, y = r \cos \theta)$ plane at different time instants. The slanted line shows the jet boundary ($\theta = \theta_j$). Darker shade indicates higher luminosity values.

conclusion. As is evident from Fig. 6, the shock-front velocity is supersonic and our analysis shows that the Mach number of the shock front, $M_{sh} = v_{sh}/c_a$, does not change with radius. We believe that this increase of the velocity of the shock fronts with increasing radius can be explained by the combined effect of two factors. First, the development of instability with the distance from the center. Second, the well-known effect of the acceleration of the shock as it propagates toward decreasing density, because the distribution of the gravitational potential (7) adopted in our model implies that $\rho \propto r^{-3}$.

Figure 7 demonstrates the evolution of the relative perturbations of luminosity normalized to its equilibrium value. The propagation of shocks from the jet boundary into the ambient medium is immediately apparent.

Let us dwell on the following point, which is of great importance for our analysis. A characteristic feature of the systems with Newtonian-type gravitational potentials (protostars) is that perturbations born in the jet encompass the entire surrounding “atmosphere”. This is due

to impedance in the atmosphere being lower than in the jet: $\rho_a c_a < \rho_j c_j$. That is why we can assume that in a protostar-type accretion-jet system the jet and the accretion disk interact through waves in the atmosphere (Levin et al., 1999). In our model, we have a reverse situation: $\rho_a c_a > \rho_j c_j$, which prevents the penetration of perturbations into the ambient medium. In this case, shocks propagate inside a limited cone with the half-opening angle of θ_{cone} about the central jet.

Figure 8 shows the dependence of the characteristic depth of such a penetration in latitude θ ($\theta_{cone} - \theta_j$) as a function of time. As is evident from this figure, θ_{cone} first increases rapidly with time and then reaches saturation. Note that this effect — localization of perturbations in the ambient medium inside a wide cone around the jet — does not depend on the mode type, because impedance is independent of the particular type of wave symmetry (symmetric or helical). Moreover, we argue that this effect is also independent of the physical mechanism of mode excitation. This means that perturbations of both vol-

ume resonance modes due to superreflection and Kelvin–Helmholtz surface modes decrease equally rapidly in the ambient medium with the distance from the jet boundary.

As is evident from Fig. 8, the opening angle of the cone overtaken by perturbations exhibits quasi-periodic damped oscillations. This behavior is due to the above-mentioned nonlinear superposition of two modes with different physical buildup mechanisms. These modes have different frequencies and, correspondingly, beating shows up at the half-difference frequency superimposed on the carrier frequency equal to the half-sum of the mode frequencies. After reaching nonlinear saturation, the KHI begins to smoothly decay and so does beating, and subsequent evolution is determined by the dynamics of the volume resonance mode $n_j = 0$. Quasi-periodic oscillations show up most conspicuously in the contours of radially-averaged perturbations drawn in the “latitude — time” plane (see Fig. 9).

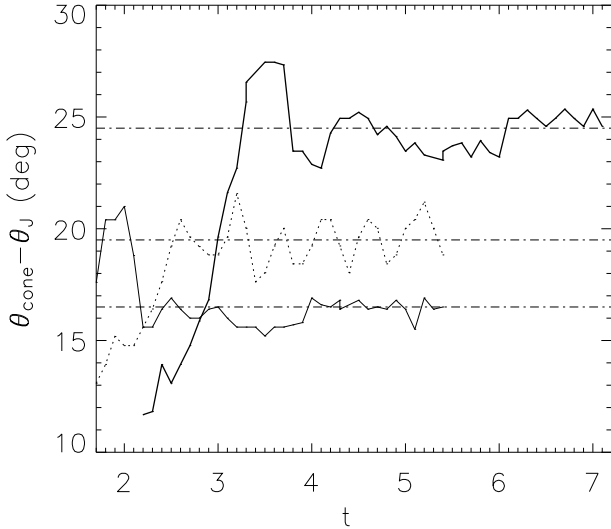


Fig. 8. Time dependence of the opening angle of the conical domain overtaken by perturbations. The bold solid line shows the results of the simulations with a 256×128 grid, $\theta_j = 10^\circ$, $\tau = 2$, and $\tilde{R} = 10$. The thin solid line shows the results of the simulations with a 256×256 grid, $\theta_j = 5^\circ$, $\tau = 4$, and $\tilde{R} = 10$. The dashed line shows the results of the simulations with a 256×256 grid, $\theta_j = 5^\circ$, $\tau = 4$, $\tilde{R} = 5$.

Oscillations are due to yet another effect. Heating of gas in shocks changes the dispersion law. This results in the decrease of the flux of energy transferred to perturbations due to the development of instability, and the decrease of the perturbation amplitude. Subsequent radiative cooling causes the relaxation of gas to a close-to-equilibrium state, the dispersion law is restored, and the perturbation amplitude grows again. Both processes described above (beating and quasi-periodic variations of the dispersion law) are essentially nonlinear and difficult to decouple from each other.

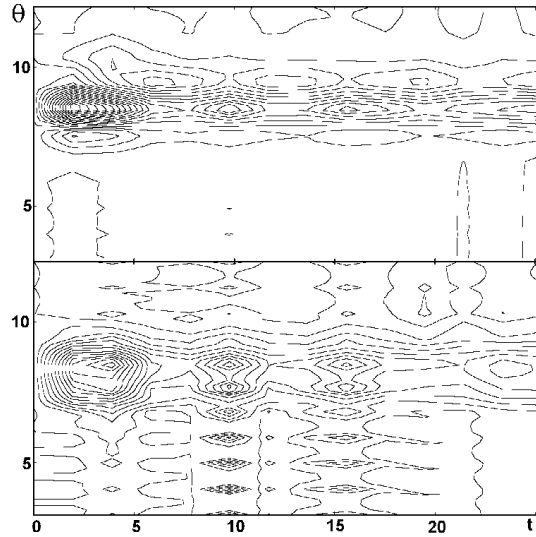


Fig. 9. Contours of radially-averaged distributions of temperature $(T(t) - T(0))/T(0)$ (top) and the θ -component of velocity $W(t)$ (bottom).

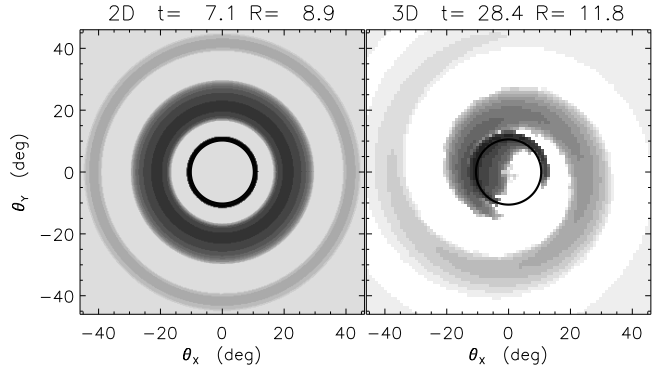


Fig. 10. Cross sections of the volume-density cone at the constant-radius level. Dark shades correspond to maximum-brightness regions. Left-hand panel shows the axisymmetric mode in the 2D simulation (the luminosity cone obtained by rotating the computed domain about the $\theta = 0$ axis). The right-hand panel shows the first helical mode according to the results of 3D simulations. The central circle corresponds to the jet boundary. The corresponding radius and time are indicated above each figure.

3.3. Results of 3D Simulations

In the case of 3D simulations we are forced to restrict our analysis to a $128 \times 64 \times 32$ grid, which is rather coarse in terms of the θ and φ angles. Therefore the growth of perturbations due to the effect described in Section 3.2 was much slower than in the case of 2D simulations and ceased at lower relative amplitudes. It is, however, safe to say that all the basic patterns of the evolution of perturbations are the same as in the two-dimensional case and therefore here we discuss only the aspects that differ.

First, in the case of 3D simulations we analyzed the development of the first helical ($m = 1$) mode until the development of shocks. In the constant- r cross section the

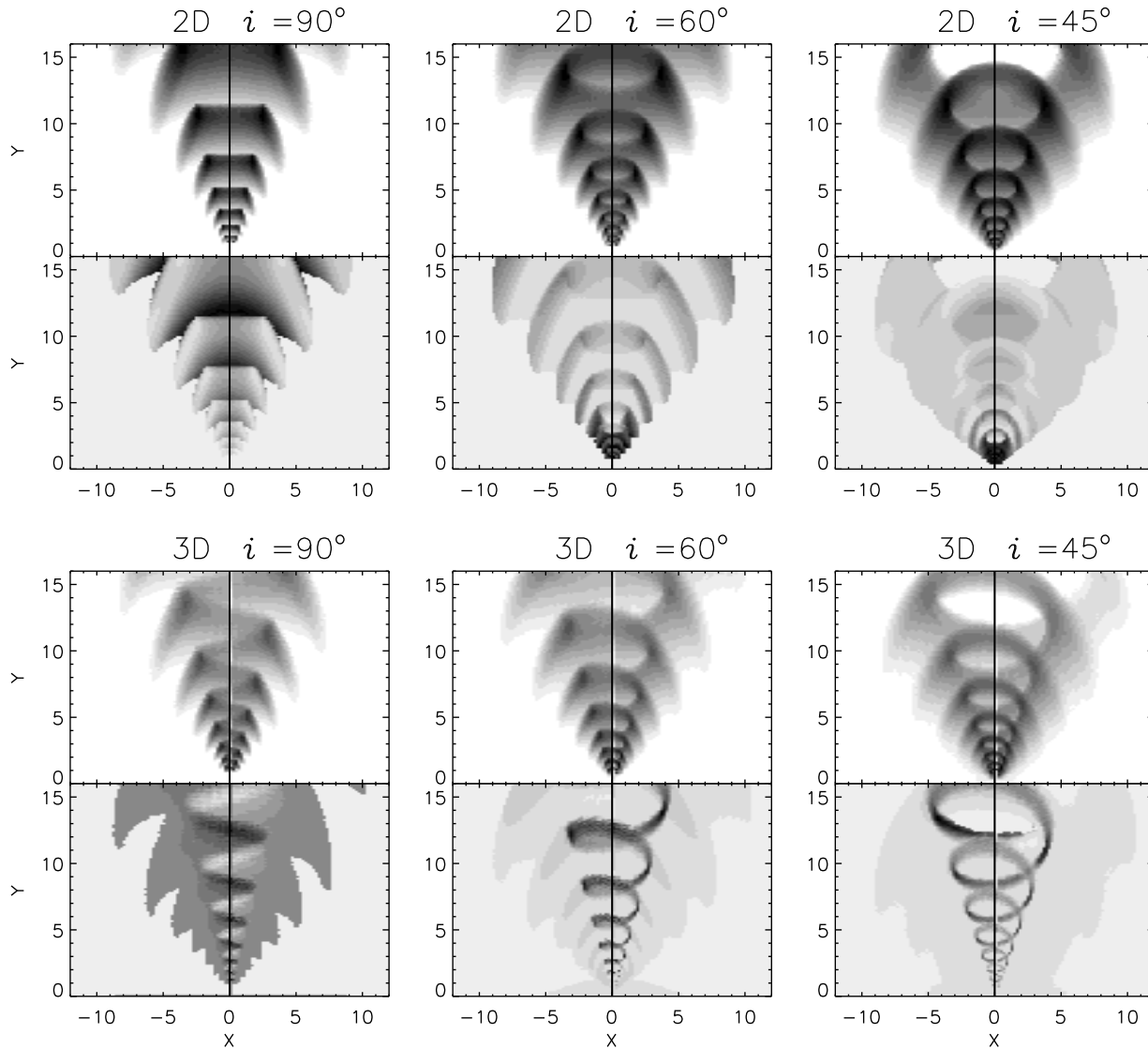


Fig. 11. Sky-plane projection of emission-line cones for different tilt angles i between the line of sight and cone axis. The upper block of figures shows the results of 2D simulations (axisymmetric perturbations). The lower block of figures shows the results of 3D simulations (the first helical mode of perturbations). The upper maps show the luminosity (surface density) maps and the lower maps correspond to radial-velocity fields in arbitrary scale.

wave pattern of this mode has the form of a one-armed trailing (relative to the rotation of the phase pattern) spiral — see Fig. 10. In three dimensions this pattern has the form of a slowly rotating (compared to Ωr) helical structure filling a wide cone around the central collimated jet.

We constructed a series of simulated wave-pattern surface brightness maps (“emission-line images”, see Section 3.1) for different tilt angles i of the cone axis to the line of sight. We also constructed the velocity fields, i.e., the maps of luminosity-weighted line-of-sight gas velocities. Figure 11 shows examples of such maps separately for the symmetric and helical patterns.

It is evident from the figures that the sky-plane projections of the three-dimensional helical pattern depend on angle i , allowing both the Z -shaped and loop-shaped emission-line patterns to be obtained. The rotation of

this phase feature on the radial-velocity map results in switching from “red” to “blue” shift to be observed as we pass from one arm of the Z -shaped pattern to another (Fig. 12). We pointed out in the “Introduction” to Paper I that such a velocity behavior is typical of some galaxies with Z -shaped emission-line features. In our model switch of velocities is explained first and foremost by the rotation of the wave pattern inside the cone.

3.4. Astrophysical Applications

Thus our simulations show that instabilities of highly collimated jets emerging from active galactic nuclei result in the propagation of shocks from the jet boundary into the ambient medium. These shock waves are located in the cone with a half-opening angle of $15^\circ \div 40^\circ$ outside

the jet. It is evident that in actual situations the ionized gas behind the shock should radiate intensively in optical lines (H_α , [OIII] etc.). A rather short-wavelength structure forms — $kr \simeq 15 - 20$ — and hence even a relatively small tilt of the symmetry axis of the cone considered with respect to the observer would produce a projection effect making the structure to appear as a continuous radiation cone with brighter regular features — “arcs” for axisymmetric wave modes or a Z-shaped pattern for the first helical mode — superimposed on it.

In Fig. 11 we sketchy reproduce the situation described based on the results of our simulations for three different tilt angles of the cone symmetry axis to the line of sight and show the distribution of luminosity integrated along the line of sight (thus the adopted model assumes optical transparency of gas). It goes without saying that in real galaxies one has to take into account dust absorption behind the shock fronts. Thus the images of ionization cones reported by Ferruit et al. (1998) and Quillen et al. (1999) exhibit extended dust lanes associated with regular structures inside the cones.

The proposed scenario of the formation of ionized cones makes it also possible to describe to a first approximation the radial-velocity pattern observed in these cones. In the previous section we already explained velocity switching inside a Z-shaped emission-line structure due to a rotating helical wave. At the same time, the velocity fields of some Seyfert galaxies exhibit only “blue” Doppler shifts in one ionization cone and only “red” shifts in the diametrically opposite cone. A good example is provided by the NGC 5252 galaxy whose velocity field was published by Morse et al. (1998) and Moiseev et al. (2000). Below we show that such a behavior can be explained by the development of an axisymmetric wave mode.

Indeed if the tilt angle of the radio-jet axis to the line of sight $\alpha \simeq 30 - 60^\circ$, then the cone nearest to the observer should be seen through shock fronts propagating virtually toward the observer and the farthest cone, against receding shock fronts (see Fig. 12). It is evident from Fig. 6 that the velocities of these fronts can be estimated as:

$$\begin{aligned} v_{sh} &\simeq (1.2 \div 1.6)c_a = (1.2 \div 1.6) \frac{U_j}{\sqrt{\bar{R}M}} = \\ &= (1.2 \div 1.6) \frac{3\Omega r}{\sqrt{\bar{R}M}}. \end{aligned} \quad (9)$$

We now substitute the numerical values quoted in 2.3 into (9) to determine

$$v_{sh} \simeq (150 - 630) \text{ km s}^{-1},$$

which agrees well with the observed Doppler shifts (see references to Paper I). Moreover, the velocities of shock fronts increase linearly with radius (see Fig. 6), implying that the Doppler shift of radial velocities should also increase with the distance from the nucleus.

In Fig. 13 we compare the [OIII]-line image of the NGC 5252 galaxy (contour image in Fig. 1 from Paper I) and examples of arbitrarily scaled simulated images for the modes with $m = 0$ and $m = 1$.

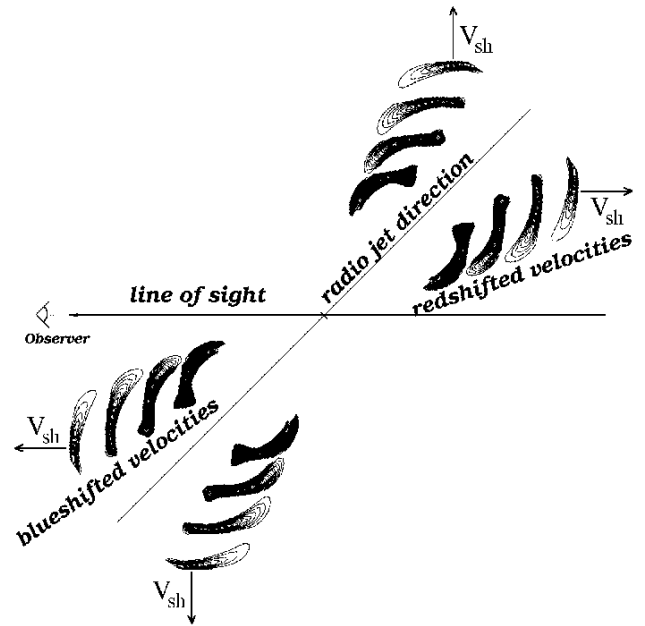


Fig. 12. A diagram explaining the formation mechanism of the observed velocity field in the case of the development of an unstable axisymmetric mode. We adopted the shock fronts in the $r - \theta$ plane from the results of our 2D simulations for dimensionless time instant $t = 10$.

Note that our simulations were either axisymmetric or nonaxisymmetric. However, in real situations pinch perturbations and helical modes in the jet develop simultaneously. Nonlinear superposition of such modes can explain the morphology of the wave pattern and the velocity field observed in the NGC 5252 galaxy if we assume that the helical and axisymmetric (pinch) mode dominate in the inner and outer parts, respectively.

4. DISCUSSION AND CONCLUSIONS

- Results of our nonlinear numerical simulations qualitatively confirm the conclusions based on linear analysis made in Paper I.
- The development of the waveguide-resonance instability of internal gravity modes in a highly collimated jet outflow from the galactic nucleus may result (in the domain controlled by the gravity of the bulge) in the formation of a short-wavelength ($kr \simeq 15 - 20$) periodic system of shocks (Mach cones) in the matter surrounding the jet.
- The shock structure mentioned above embraces a wide cone with a half-opening angle of $\theta_c \simeq 15^\circ - 40^\circ$. The opening angle of the cone is determined by particular parameters of the outflow (first and foremost, by the ratio of the impedances of the jet and the ambient gas).
- Given the intense radiative cooling of gas behind the shock fronts and projection effects, it can be assumed that the shock system discussed here must appear to the observer as a wide radiation cone with a wave pattern superimposed. In this case, helical modes deter-

mine the appearance of Z-shaped emission-line structures observed in a number of Seyfert galaxies.

Note that a number of authors already solved a similarly formulated problem (see, e.g., Rossi et al., 2000; Lim & Steffen, 2001; Hardee, 2003), however, they analyzed an earlier stage of the interaction between the jet and the surrounding gaseous clouds. A “cocoon” does indeed form behind the bow shock when a supersonic jet intrudes into the ambient medium. This effect was demonstrated many times in numerical simulations and one can see it on images made with the Hubble Space Telescope, e.g., in the central region of Mrk 3 (Capetti et al., 1999) or Mrk 78 (Whittle et al., 2004). However, on longer spatial scale lengths ($r > 0.5 - 1$ kpc), like in the case of NGC 3516, Mrk 573, and NGC 5252 (see images in Paper I), no such shock is observed. This unambiguously proves that the initial injection of the jet (which formed deep in the inner region of the system in the accretion torus around the black hole) occurred rather long ago. We believe that in these objects the jet has already punched a channel in a more or less dense medium in the central region of the galactic disk, and the bow shock has broken into the intergalactic medium (like this happens with galactic fountains). Since then, the gas of the cocoon must have relaxed (at least partially) and it must interact with the jet over the scale lengths mentioned above, leading to instability. On long scale lengths the jet propagates ballistically, however, its gas loses energy as a result of radiative cooling and there are no new mechanisms for the buildup of oscillations (because of the extremely low density of the ambient medium), implying that gas does not show itself in any observable way. We simulated exactly this situation. Note the instability of this type may develop even in the absence of a sharp jet boundary. It is sufficient for the supersonic velocity difference to occur over less than one wavelength, and there will always be such perturbations.

We understand that our model is only a first step toward the construction of the pattern of regular structures in ionization cones. When constructing a self-consistent model of such objects one must take into account at least the following factors:

- Contributions of the flat (large-scale disk) and triaxial (bar) subsystems.
- Rotation of the galactic nucleus.
- Slow rotation of the matter of the conical jet about its symmetry axis.
- Interaction between the jet and the ambient gas of the disk (in the case of a small angle between the jet and the disk plane.
- The presence inside the shock of a “cocoon” produced by the supersonic intrusion of gas of the conical outflow into the dense gas of the disk.

We believe the above factors to be of great importance for the dynamics of various concrete objects, however, they do not determine the essence of the phenomenon and therefore we ignored them in this paper. However, when

discussing the formation of the observed structures in concrete objects one has to take most of the above factors into account.

In addition, to conclude our discussion, we point out that collimated jet outflows from active galactic nuclei leave the bulge region after having acquired an essentially nonlinear, shock structure. Let us also add that near the bulge region (in the sense that the gravitational potential is dominated by the spherically symmetric part) this structure must undergo significant changes due to rather sharp change of the law of the distribution of the gravitational potential and hence that of pressure and density inside the jet and in the ambient medium.

Acknowledgements. We are grateful to V.V. Levi and A.V. Nikitin for their assistance and numerous useful discussions. A.V. Moiseev and V.L. Afanasiev acknowledge the support of the Russian Foundation for Basic Research (project no. 06-02-16825). We thank the reviewer Torgashin Yu.M. for valuable remarks that improved this paper.

References

- Afanasiev V.L., Dodonov S.N., Khrapov S.S., Moiseev A.V., Mustsevov V.V., 2007, *Astrophysical Bulletin* **62**, 3 (Paper I), astro-ph/0702636
- Bodo G., Rosner R., Ferrari A., Knobloch E., 1989, *ApJ*, **341**, 631
- Capetti A., Axon D.J., Macchetto F., Marconi F.D., Winge C., 1999, *ApJ*, **516**, 187
- Falcke H., Wilson A.S., Simpson C., Bower G.A., 1996, *ApJ*, **470L**, 31
- Ferruit P., Wilson A.S., Mulchaey J.S., 1998, *ApJ*, **509**, 646
- Hardee P., 1982, *ApJ*, **257**, 509
- Hardee P., 2003, *ApJ*, **597**, 798
- Lim A.J., Steffen W., 2001, *MNRAS*, **322**, 166
- Levin, K.A., Mustsevov, V.V., Khrapov, S.S., 1999, *Astro. Report*, **43**, 104
- Lobanov A.P., Krichbaum T.P., Witzel A., Zensus J.A., 2006, *PASJ*, **58**, 253
- Moiseev A.V., Afanasiev V.L., Dodonov, S.N., Khrapov, S.S., Mustsevov, V.V., 2000, poster presented on JENAM-2000, astro-ph/0006323
- Morse J. A., Cecil G., Wilson A.S., Tsvetanov Z.I., 1998, *ApJ*, **505**, 159
- Mustsevov V.V., Khoperskov A.V., 1991, *Soviet. Astronomy. Letters*, **17**, 119
- Nagar N.N., Wilson A.S., Mulchaey J.S., Gallimore J.F., 1999, *ApJS*, **120**, 209
- Quillen A.C., Alonso-Herrero A., Rieke M.J., et al., 1999, *ApJ*, **525**, 685
- Rossi P., Capetti A., Bodo G., Massaglia S., Ferrari A., 2000, *A&A*, **356**, 73
- Ryu D., Ostriker J.P., Kang H., Cen R., 1993, *ApJ*, **414**, 1
- Whittle M., & Wilson A.S., 2004, *AJ*, **127**, 606

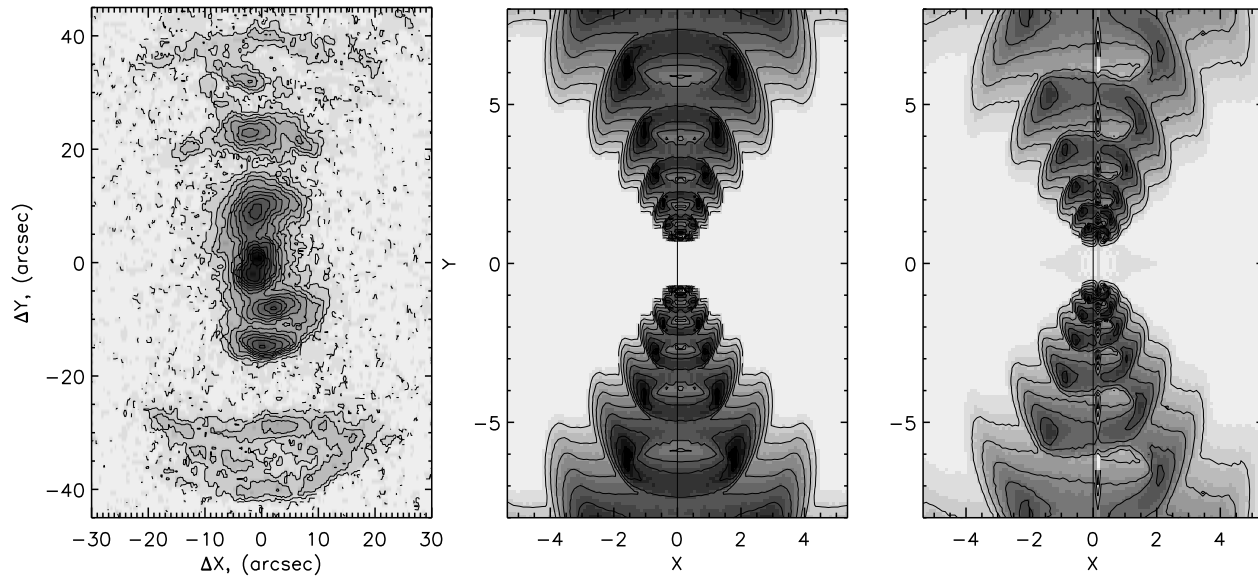


Fig. 13. Left-hand panel: an [OIII]-line contour image of the NGC 5252 galaxy. Central panel: simulated velocity map for the pinch mode ($m = 0$) $i = 60^\circ$. Right-hand panel: simulated luminosity map for the helical mode ($m = 1$) $i = 60^\circ$.

This figure "fig1.jpg" is available in "jpg" format from:

<http://arxiv.org/ps/astro-ph/0702639v1>

This figure "fig2.jpg" is available in "jpg" format from:

<http://arxiv.org/ps/astro-ph/0702639v1>

This figure "fig3.jpg" is available in "jpg" format from:

<http://arxiv.org/ps/astro-ph/0702639v1>

This figure "fig4.jpg" is available in "jpg" format from:

<http://arxiv.org/ps/astro-ph/0702639v1>